



Manufacturing and Virtual Design to Tailor the Properties of Boron-Alloyed Steel Tubes

Illia Hordych, Sebastian Herbst, Florian Nürnberg, Viacheslav Boiarkin,
Olivier Hubert, Hans Jürgen Maier

► To cite this version:

Illia Hordych, Sebastian Herbst, Florian Nürnberg, Viacheslav Boiarkin, Olivier Hubert, et al.. Manufacturing and Virtual Design to Tailor the Properties of Boron-Alloyed Steel Tubes. Peter Wriggers; Olivier Allix; Christian Weißenfels. Springer International Publishing, 93, pp. 21-44, 2020, Lecture Notes in Applied and Computational Mechanics, Virtual Design and Validation, 10.1007/978-3-030-38156-1 . hal-02559686

HAL Id: hal-02559686

<https://hal.science/hal-02559686>

Submitted on 30 Apr 2020

HAL is a multi-disciplinary open access archive for the deposit and dissemination of scientific research documents, whether they are published or not. The documents may come from teaching and research institutions in France or abroad, or from public or private research centers.

L'archive ouverte pluridisciplinaire **HAL**, est destinée au dépôt et à la diffusion de documents scientifiques de niveau recherche, publiés ou non, émanant des établissements d'enseignement et de recherche français ou étrangers, des laboratoires publics ou privés.

Manufacturing and Virtual Design to Tailor the Properties of Boron-Alloyed Steel Tubes

Illia Hordych¹, Sebastian Herbst¹, Florian Nürnberg¹, Viacheslav Boiarkin², Olivier Hubert³, Hans Jürgen Maier¹

¹Institut für Werkstoffkunde (Materials Science), Leibniz Universität Hannover, Germany

²Department of Metal Forming, National Metallurgical Academy of Ukraine, Ukraine

³Laboratoire de Mécanique et Technologie, Ecole Normale Supérieure Paris Saclay, France

Abstract Application of products with properties locally adapted for specific loads and requirements has become widespread in recent decades. In the present study, an innovative approach to manufacture tubes with tailored properties in the longitudinal direction from a boron-alloyed steel 22MnB5 was developed. Due to advanced heating and cooling strategies, a wide spectrum of possible steel phase compositions can be obtained in tubes manufactured in a conventional tube forming line. A heat-treatment station placed after the forming line is composed of an inductive heating and an adapted water-air cooling spray system. These short-action processes allow fast austenitizing and subsequent austenite decomposition within several seconds. To describe the effect of high inductive heating rates on austenite formation, dilatometric investigations were performed in a heating rate range from 500 K s^{-1} to 2500 K s^{-1} . A completed austenitizing was observed for the whole range of the investigated heating rates. The austenitizing was described using Johnson-Mehl-Avrami model. Furthermore, series of experiments on heating and cooling with different cooling rates in the developed technology line was carried out. Complex microstructures were obtained for the cooling in still as well as with compressed air, while the water-air cooling at different pressures resulted in quenched martensitic microstructures. Nondestructive testing of the mechanical properties and the phase composition was realized by means of magnetization measurements. Logarithmic models to predict the phase composition and hardness values from the magnetic properties were obtained. Subsequently, a simulation model allowing virtual design of tubes in the FE-software ANSYS was developed on basis of experimental data. The model is suited to predict microstructural and mechanical properties under consideration of the actual process parameters.

Introduction

In the pursuit of economic and ecologic manufacturing processes, different products that can be adapted to local loadings and stresses have been developed. From this point of view, tailored components are attractive due to the possibility of their local adjustment to application purposes. Different technological strategies can be employed in order to tailor the mechanical properties of products [1], which can be divided into two main groups: in the first one, tailoring is achieved by combining materials with different properties. In this case, dissimilar materials are combined through the creation of metallurgical, form- or force-closed joints depending on their unique characteristics [2, 3]. The second group assembles methods of tailoring properties within the same material through the adaptation of geometry dimensions (e.g. rolling with alternating roll diameters) and/or microstructures (e.g. selective heat-treatment) [4]. A break-through in the industry of, above all, automotive steels that came with introduction of complex microstructures (dual-, complex-phase, TRIP-, TWIP-steels) attracted strong attention to advanced heat-treatments and the possibility of steel tailoring through miscellaneous time-temperature courses [5, 6]. In this respect, boron and manganese alloyed steels are characterized by their enhanced hardenability and a wide spectrum of possible phase compositions achievable by heat-treatments. In addition, they exhibit a high level of mechanical and wear properties in service. [7].

The present investigation aims to develop and implement a technology line, which allows the manufacturing of tailored tubes based on locally adapted mechanical properties in the longitudinal direction by means of an advanced heat-treatment integrated in the production line. Being a continuous process, tube forming is advantageous for integration of a local heat-treatment station to manufacture hollow profiles with a constant cross-section over the length. When using boron-alloyed steels, a significant delay of ferrite-perlite formation during the cooling due to the boron addition technologically simplifies an achievement of different steel phases. Depending on the cooling rate, diffusive (ferrite-perlite, bainite) as well as diffusionless (martensite) transformations can take place [8]. This implies that by a selective heat-treatment and adapted heating/cooling strategies, different combinations of phase compositions can be obtained, such as relatively ductile ferrite-perlitic or bainitic and hard martensitic sections. Such tailored tubes can:

- be post processed as semi-finished products: for the manufacturing of, e.g. T-shape tubes by means of hydroforming, certain sections to be processed can be held purposely ductile, while not affected sections will gain the final properties during the integrated heat-treatment.
- find a direct application: for instance, ductile sections of frame rails in the automotive body can absorb the kinetic energy during a crash accident and hence, ensure a controlled deformation through a predictable folding, whereas hard sections remain responsible for the crash resistance. In addition, a damping effect of ductile sections can enhance vibration resistance of these products.

To reduce the experimental and costs efforts, a simulation model allowing to predict optimal heating and cooling parameters in dependence on the required finish properties of the tube under consideration of the actual process parameters was developed within this study.

Material

The current work is focused on the investigations performed with a boron alloyed heat treatable steel 1.5528 (22MnB5). It has been widely applied for the press-hardening since the mid-1990s due to its remarkable properties during processing [9] (Fig. 1): these provide an increased deformability in the hot state with an extended temperature range for hot forming as well as an enhanced hardenability during cooling. An addition of boron in quantities between 0.008 and 0.030 wt.-% facilitates formation of a quenched microstructure through the delay of the diffusive decomposition of austenite in steel. While the tensile strength in the as-delivered state is about 600 MPa, it reaches more than 1500 MPa in the quenched state.

As determined by atomic emission spectroscopy, the chemical composition of the used steel charge is in accordance with the norm values [10]: C – 0.23, Si – 0.30, Mn – 1.23, Cr – 1.16, Ti – 0.04, B – 0.0031, balance Fe, in wt.-%. In the initial as-delivered state, it consists of ferrite – white areas in Fig. 1 – and perlite – black spots in Fig. 1.

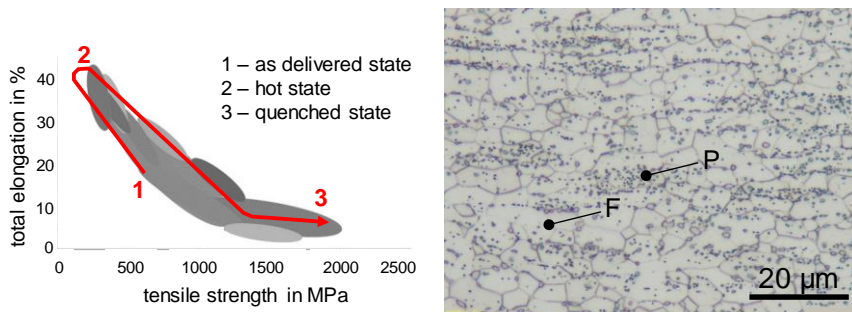


Fig. 1. Evolution of the mechanical properties during hot-stamping (left) and initial microstructure of the steel 22MnB5 used within the present study in the as-delivered state (right).

The metallographic preparation is equal for all investigations in the present study. The samples were embedded, ground and polished to 1 μm diamond paste finish. Surfaces were etched with 1% HNO₃ for 2 s to contrast the individual phases.

Technological process

The developed technology is based on a traditional tube forming line, which consists of three processing stages – sheet forming, welding and sizing (Fig. 2a). With 16 (13 forming and 3 sizing) multi-roll stands, a metal sheet is incrementally closed to a circle profile, which is welded and sized in terms of improved surface properties. At the end of the line, a number of profiling stands is positioned for adjustment of the profile cross-section if necessary. The tube forming is realized using a laboratory scale electric pipe-welded profiling machine “Nagel Profiliertechnik 1001”. With a given roll pass design, it allows manufacturing of tubes with an outer diameter of 20 mm from a metal strip with a thickness between 0.5 mm and 0.8 mm (Fig. 2b). An available feed range from 0.01 mm s^{-1} to 250 mm s^{-1} is limited by the welding process. A plasma arc welding station “EWM Microplasma 50” integrated in the production line provides a maximal current of 50 A. This welding type uses plasma gags to melt preformed steel edges without any filler materials, which is advantageous for a continuous line in terms of absent flash in the welded zone. Preliminary investigations of the welding parameters resulted in sufficient welding seam properties at feed rates up to 50 mm s^{-1} .

The described conventional tube forming line is upgraded with an advanced heat-treating station (Fig. 2c). An inductive heating and a subsequent water-air spray cooling are short-acting methods and thus, advantageous to be applied in the line. The heating and cooling ensures high process rates to enable the required transformations in a few seconds. Following the tube forming stands, an induction coil is installed in the production line to heat up the welded tube. An available medium frequency inductor “Eldec MFG 30” can generate a maximal power of 30 kW and thus provide a wide range of heating rates. Subsequently, an water-air spray cooling system is positioned. It consists of two independent water-air circles with four spray nozzles per circle. A flexible setup and control system of the heating/cooling conditions offers various strategies to produce complex microstructures and hence tailored properties [11].

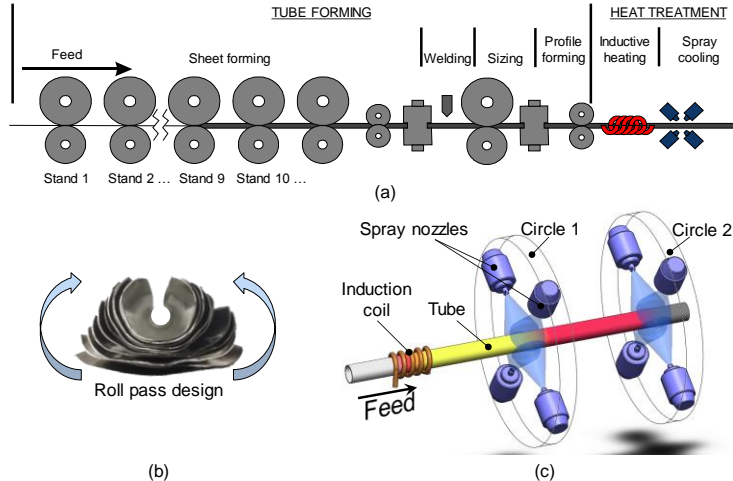


Fig. 2. Schema of the tube forming line (a) with a given roll pass design (b) and an integrated heat-treatment station (c).

Phase transformations during heat-treatment

Austenite formation during inductive heating

The formation of different steel phases during cooling can be fulfilled exceptionally from the austenite state. Depending on the cooling rate, ferrite-perlite, bainite or martensite can occur in the steel 22MnB5. Thus, tube segments to be cooled should exhibit an austenitic microstructure. To be fully austenitized, 22MnB5 is usually exposed to a furnace heating at 850-950 °C with a soaking time between 3 min and 6 min [9, 12, 13]. However, one of the characteristic properties of continuous lines is limited time for heating and soaking. Conventional furnace heat-treatments appear to be hardly realized within a continuous process. Since austenite formation is governed by diffusion of carbon atoms into the iron lattice, steel tubes should be significantly overheated to promote diffusive processes and compensate a lack of time.

A possible range of suitable heating rates can be determined on the basis of the technical properties and parameters of the line (Equation 1). Both feed rate and coil length determine the necessary heating rate to reach the required austenitizing temperature:

$$V_h = \frac{(T_A - T_R) \cdot v_p}{l_i}, \quad (1)$$

where V_h – heating rate in K s^{-1} , T_A – austenitizing temperature in $^\circ\text{C}$, T_R – room temperature in $^\circ\text{C}$, v_p – feed rate in mm s^{-1} , l_i – inductor length in mm (Fig. 3).

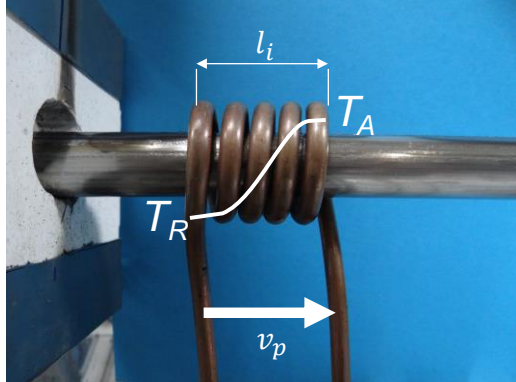


Fig. 3. Heating station with a given inductor coil and parameters determining the heating rate at a constant inductor power.

For the current study, an inductor coil with a length of 50 mm was used. The feed rate was limited by the plasma welding in the processing line. In order to accelerate the diffusion, the target austenitizing temperature was set at a value of 1150 $^\circ\text{C}$, which is above the temperature of the homogenous austenite at the highest heating rates in literature [14]. Thus, the range of relevant rates was set between 500 K s^{-1} and 2500 K s^{-1} . The inductive heating is described for heating rates up to 150 K s^{-1} in [14, 15]. The reported data does not cover the relevant heating rate range. Hence, a series of dilatometric investigations on phase transformations during rapid austenitizing were performed in a previous work of the authors [16]. Steel samples were inductively heated at the nominal rates of 500 K s^{-1} , 1200 K s^{-1} , 1800 K s^{-1} , 2500 K s^{-1} using a dilatometer DIL 805A/D+T from Bähr with three samples per rate. Without soaking, the samples were immediately quenched with compressed nitrogen at 30 K s^{-1} to capture the formed austenite fraction at an elevated temperature and indirectly confirm its formation through the martensite fraction at room temperature (critical cooling rate of 22MnB5: 27 K s^{-1}) [13].

The actual heating courses of one sample per heating rate are exemplary plotted in the logarithmic scale in Fig. 4. Two temperature ranges with different heating rates are clearly distinguishable. These are separated along the line of Curie temperature that represents the change in the magnetic properties from ferromagnetic to paramagnetic [17]. Depending on the steel grade and chemical composition, Curie temperature lies in between 720 $^\circ\text{C}$ and 768 $^\circ\text{C}$ [18]. In fact, the target heating rates were valid only up to the Curie temperature; above a drop to values between 368 K s^{-1} and 380 K s^{-1} was observed.

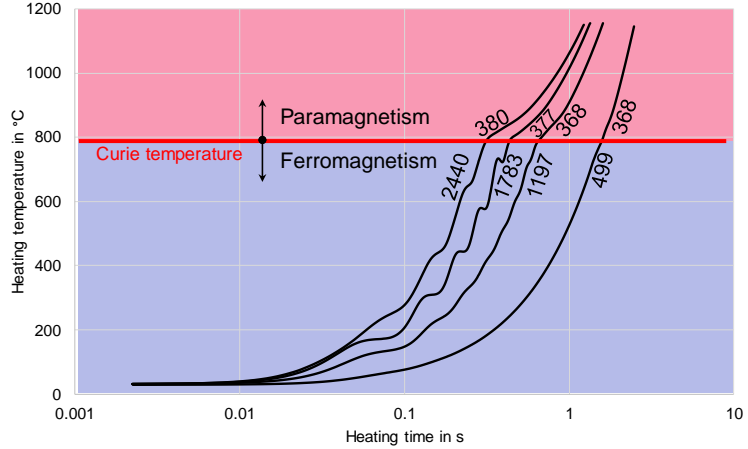


Fig. 4. Heating courses obtained during dilatometric experiments with the actual heating rates calculated below and above Curie temperature in K s^{-1} .

The obtained dilatometric curves for the inductive heating are shown in Fig. 5. For all tested heating rates, the courses appear to be similar. For a better visibility, these are manually shifted along the Y-axis by -0.1%. Due to the fact, that the transformations took place above Curie temperature, the heating rates were quite similar in this temperature range. Although this resulted in a similar transformation behavior, increasing heating rates shifted the transformation temperatures to the higher values. From the dilatometric curves, the A_{c1} - and A_{c3} -temperatures were derived. These describe the start and the finish of the transformation correspondingly. The transformation start temperatures vary between 816 °C to 832 °C, whereas the transformation finish temperatures lie in the range from 946 °C to 995 °C. In both cases, the temperatures increase with increasing heating rates. The determined parameters of the heating courses and transformation kinetics are summarized in Table 1.

Table 1. Heating and transformation parameters determined from the dilatometric investigations (T_C – Curie temperature).

Target	Heating rate in K s^{-1}			Transformation temperatures in °C	
	Real, below T_C	Real, above T_C	Average	A_{c1}	A_{c3}
500	499 ±1	368 ±1	440 ±6	816 ±6	946 ±12
1200	1197 ±2	368 ±20	709 ±12	828 ±3	974 ±15
1800	1783 ±4	377 ±17	854 ±12	826 ±4	971 ±17
2500	2440 ±13	380 ±4	898 ±26	832 ±4	995 ±10

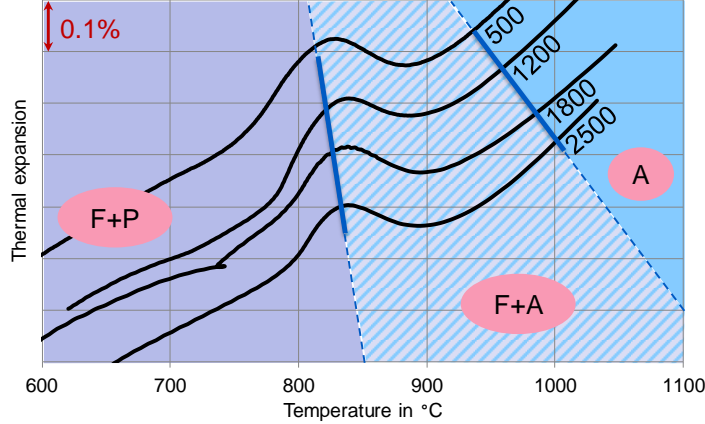


Fig. 5. Dilatometer courses for the given nominal heating rates in K s^{-1} and indication of transformation areas (F – ferrite, P – perlite, A – austenite).

The dilatometric data served as a basis for the calculations of the ferrite-perlite decomposition during the inductive heating. The method presented in [19] was implemented to describe the evolution of austenite formation as a function of heating time and heating temperature. Herein, the thermal expansion ε_{th} during heating is considered as a sum of the thermal expansions of each present phase (f_A , f_{F+P}) and the strain induced by the transformation of ferrite-perlite to austenite ε_{tr} (Equation 2):

$$\varepsilon_{th} = f_F \cdot \varepsilon_{th,F} + f_A \cdot \varepsilon_{th,A} + f_A \cdot \varepsilon_{tr}, \quad (2)$$

Through the assumption that only ferrite-perlite and austenite are present in the system, the ferrite-perlite fraction can be expressed through the austenite fraction $f_{F+P} = 1 - f_A$. Furthermore, the thermal expansion of particular phases can be represented as a product of the thermal expansion coefficient and material temperature. In this case, Equation 2 is expressed in form of Equation 3:

$$f_A(T, t) = \frac{\varepsilon_{th} - \alpha_{th,F+P} \cdot T(t)}{(\alpha_{th,A} - \alpha_{th,F+P}) \cdot T(t) + \varepsilon_{tr}}. \quad (3)$$

The thermal expansion coefficients were derived from the dilatometric curves as a linear ascent of the corresponding phases in the non-transformation areas. The coefficient of ferrite-perlite was equal $(14.52 \pm 0.17) \cdot 10^{-6} \text{ K}^{-1}$, whereas it amounts to $(23.35 \pm 1.11) \cdot 10^{-6} \text{ K}^{-1}$ for austenite. Since austenite exhibits normally a larger thermal expansion than ferrite, the values are adequate to each other and to the literature [20]. The transformation strain is an imaginary thermal expansion of austenite at the temperature of 0 °C and is equal to $-0.99 \pm 0.11\%$ for the current study.

Application of Equation 3 allowed the prediction of the austenite evolution at a particular heating temperature and time at the given heating rates (Fig. 6). The

courses are vertically shifted along the Y-axis by 10% for a better visibility. The dependence on the temperature confirmed the similar transformation range and the increase of the transformation temperatures. The austenite fraction over the heating time gives the absolute time required for the austenitizing within the investigated range of the heating rates.

Furthermore, the dilatometric and calculated data for each sample was processed to describe the evolution of the austenite formation based on the half-empirical model of Johnson-Mehl-Avrami (JMA) [21, 22]. This is usually applied to describe diffusional phase transformations in materials and assumes that each transformation process exhibits a sigmoidal course expressed by Equation 4:

$$f_A = 1 - \exp[-(kt)^n], \quad (4)$$

where t is time counted from the begin of a transformation in s; k and n – are coefficients depending on material, temperature (isothermal transformation) or heating/cooling rate (continuous transformation).

The coefficients k and n are determined as follows:

- through the mathematical transformation of the JMA-equation, it becomes evident that the moment of time, when $t = \frac{1}{k}$, corresponds to an austenite fraction of 0.6321. The interpolation of this point in the coordinate system austenite-heating time allows the identification of the corresponding time and hence, coefficient k .
- JMA-equation expressed in form of Equation 5:

$$\ln \ln \left(\frac{1}{1-f_A} \right) = n \cdot \ln(t) + n \cdot \ln(k), \quad (5)$$

demonstrates that n is equal to a slope of the function $\ln \ln \left(\frac{1}{1-f_A} \right)$ over the transformation time plotted in the logarithmic scale.

The courses of the austenite fraction as a function of temperature and heating time according to the JMA-model are exemplary plotted in Fig. 6. A good correspondence of the calculated dilatometric data and JMA-model can be stated with a slight deviation on the final transformation stages. The calculated coefficients k and n are presented in Table 2. These change only slightly; however, a tendency to decrease with increasing heating rates can be observed with an exception of n for 2500 K s^{-1} .

Table 2. Rate dependent coefficients k and n in JMA-equation for the given heating rates.

Heating rate in K s^{-1}	500	1200	1800	2500
k	5.467	5.241	5.203	4.695
n	2.025	1.903	1.885	2.336

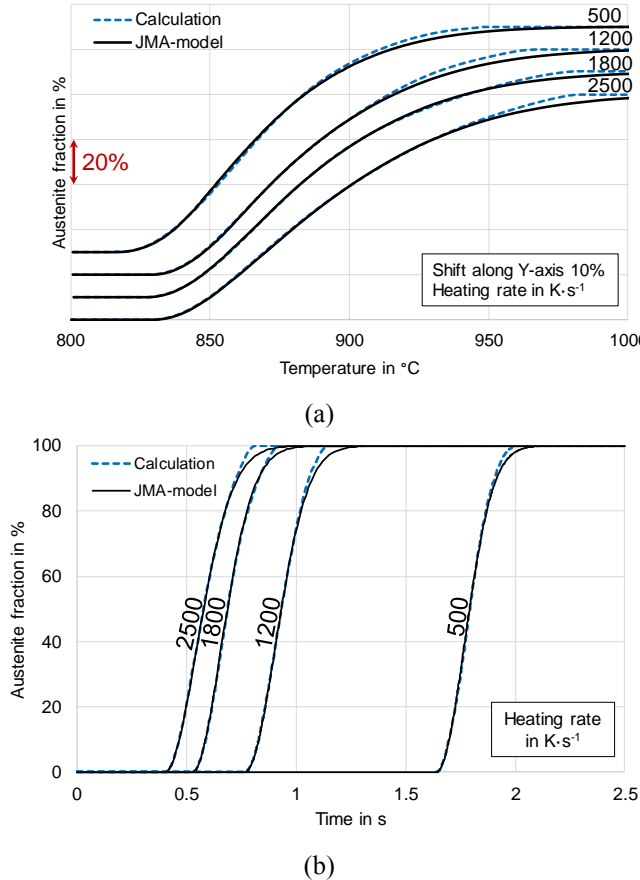


Fig. 6. Evolution of the austenite formation during the inductive heating with the given heating rates depending on (a) temperature – shift along the Y-axis of 10% - and (b) time from the start of the heating process according to calculated dilatometric data and to JMA-model.

The dilatometric investigations and performed calculations were verified by means of optical microscopy by a microstructure analysis of the tested samples. All heated and subsequently quenched samples – independent on the cooling rate – exhibit a martensitic microstructure. This reveals that a full austenitizing was achieved during the inductive heating for each heating rate. An optical micrograph of the sample heated with a rate of 2500 K s⁻¹ is exemplary depicted in Fig. 7.

The obtained dilatometric data revealed that heating above 1200 °C should ensure a full austenitizing of the tube cross-section at high heating rates during in-line-experiments in the tube forming line.



Fig. 7. Exemplary micrograph of the dilatometric sample exhibiting martensitic microstructure after heating with rate of 2500 K s^{-1} and immediate quenching with a rate of 30 K s^{-1} .

Austenite decomposition during spray cooling

Depending on the application purpose, tailored products can be of high interest in a wide range of mechanical properties. Using the advanced spray cooling, a wide spectrum of cooling rates can be obtained in the range from air cooling up to the quenching under a high water-air pressure (Fig. 8). The pressure can be adjusted in the range between 0 MPa and 0.6 MPa for both air and water flow independently. The actual temperature-time-course, which depends on the feed rate, is influenced by the inductive heating (H) and two stages of active cooling in the water-air circles (C1, C2). In addition, the tube is passively cooled on air during transports and after passing the second circle (T1-T3). The distance between the cooling circles can be flexible adjusted and will be a subject of future studies. For the present investigations, the distances corresponding to T1 and T2 are chosen to be 150 mm. Four spray nozzles per circle are positioned in the perpendicular plane to the tube feed with a tangential rotation of 45° to each other (Fig. 2c). In case of four nozzles and tubes with a diameter of 20 mm, a distance of 40 mm from a nozzle nose to the normal plane of the tube surface should ensure a complete covering of the whole cross-section with the water-air mixture [23]. Depending on the cooling intensity, all steel phases (with exception of retained austenite due to a low content of carbon) can be expected.

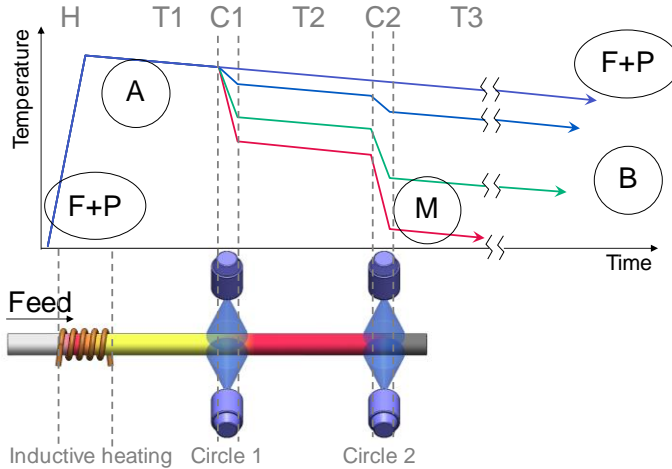


Fig. 8. Possible heat-treatment strategies to obtain different phase compositions under consideration of the parameters of the heat-treatment station (H – heating; T1, T2, T3 – air transportation stages; C1, C2 – water-air spray cooling circles).

In order to investigate the austenite decomposition during spray cooling in the technology line, a series of experiments with various cooling parameters was performed. Preliminary investigations on the inductive heating revealed the inductor power needed for reaching the austenitizing temperature. At a feed rate of 16.7 mm s^{-1} , the required temperature range can be reached using an inductor power of 12 kW. The temperature was measured with a thermocouple attached to the internal tube surface. These heating parameters were used as default for the investigations on heat-treatments with different cooling strategies. After the heating, tube segments of a length at least 150 mm were cooled on air (0 MPa water, 0 MPa air); with compressed air (0 MPa water, 0.6 MPa air) and with a water-air mixture at pressures of 0.1 MPa, 0.3 MPa and 0.6 MPa respectively. For the ease of convenience, the tube samples are named based on the corresponding cooling conditions: “XWYA”, where “X” and “Y” are accordingly equal to the water and air pressure in MPa.

The time-temperature courses of two boundary cases, namely air cooling (0W0A) and water-air cooling at 0.6 MPa (0.6W0.6A), are exemplary depicted in Fig. 9. Both heating sections exhibit a similar behavior with a higher rate below Curie temperature and a lower rate above. The accurate Curie temperature for a particular case could not be determined, since heating courses do not have pronounced inflection points. The reason may be that in the case of a continuous process, in addition to the inductive influence, the tube is heated by a heat transfer from the already austenized front sections. Preliminary experiments on the static inductive heating confirmed this presumption: without movement of the tube, the inflection point could be clearly distinguished.

An average heating rate above 500 K s^{-1} allowed reaching the maximal temperature above 1200°C in both cases. Considering the dilatometric results, this ensures a complete formation of austenite in the heated cross-sections. The air cooling curve exhibits an exponential course with a low average cooling rate of 5 K s^{-1} between 1200°C and 200°C . In the time-temperature course of the water-air spray cooling at 0.6 MPa , the passive and active cooling stages can be clearly distinguished. The tube is cooled actively when passing circles C1 and C2 with a drastic drop of temperature and cooled passively in zones T1-T3. An average cooling rate for the whole cooling is app. 74 K s^{-1} . Hence, the cooling of the other samples was carried out within the determined range between 5 K s^{-1} on air and 74 K s^{-1} using the highest water-air pressure.

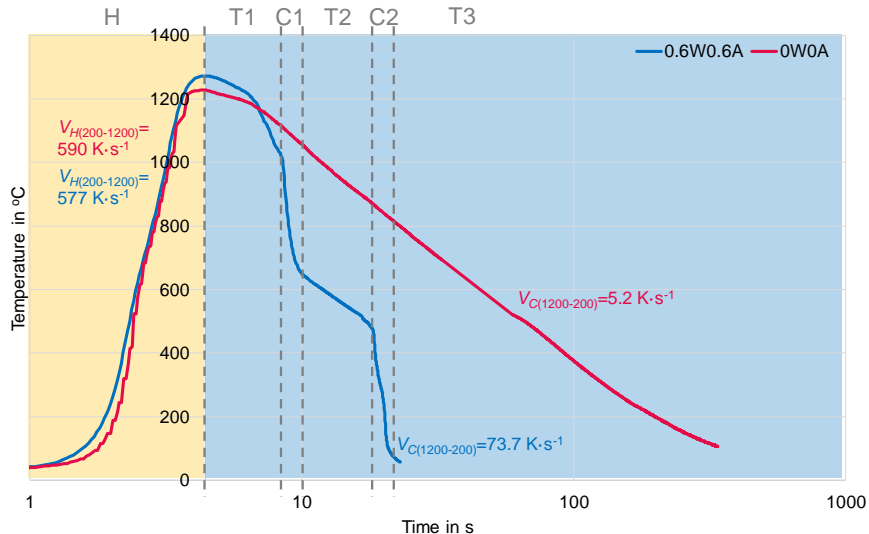


Fig. 9. Time-temperature-courses due to heat-treatments composed of inductive heating at 12 kW and spray cooling at the given cooling parameters in MPa with a feed rate of 16.7 mm s^{-1} .

After the heat-treatments, the tube samples were prepared for Vickers hardness measurements with a load force of 294.2 N (HV30) according to DIN EN ISO 6507 [24]. The hardness was measured in the longitudinal direction with a default interval of about 10 mm . The surface of the tubes was ground, polished with a fine sandpaper to remove the scale and degreased with acetone immediately before the measurement.

The average values of hardness with respective standard deviations for each specimen are depicted in Fig. 10. Increased hardness for all heat-treated samples in comparison to the initial state can be noticed. Furthermore, higher cooling rates resulted in higher hardness values correspondingly. At the beginning, the as-delivered state exhibits a hardness of 160 HV . The air cooling caused a rise to a value of 239 HV , whereas the compressed air provided a further increasing up to 352 HV . If

water is added to the air cooling mixture, the hardness grows drastically above 550 HV and then increases only slightly. There is no difference between the cooling with 0.1 MPa and 0.3 MPa in the hardness. The hardest microstructure is obtained by a water-air cooling with a pressure of 0.6 MPa.

Optical micrographs supplemented the hardness measurements. The non-treated microstructure is ferrite-perlitic: a white matrix of ferrite contains dark spots of perlite. A deformation due to the tube forming process appears not to influence the microstructure. In the air cooled samples 0W0A and 0W0.6A, inclusions of three phases could be detected: ferrite, upper and partially lower bainite. The micrographs of the samples cooled with the water-air mixture exhibit mostly martensitic microstructures independently of the water-air pressure. Hence, for the hardening the presence of water in the cooling mixture is essential and even relatively low water pressures provide a hardened microstructure.

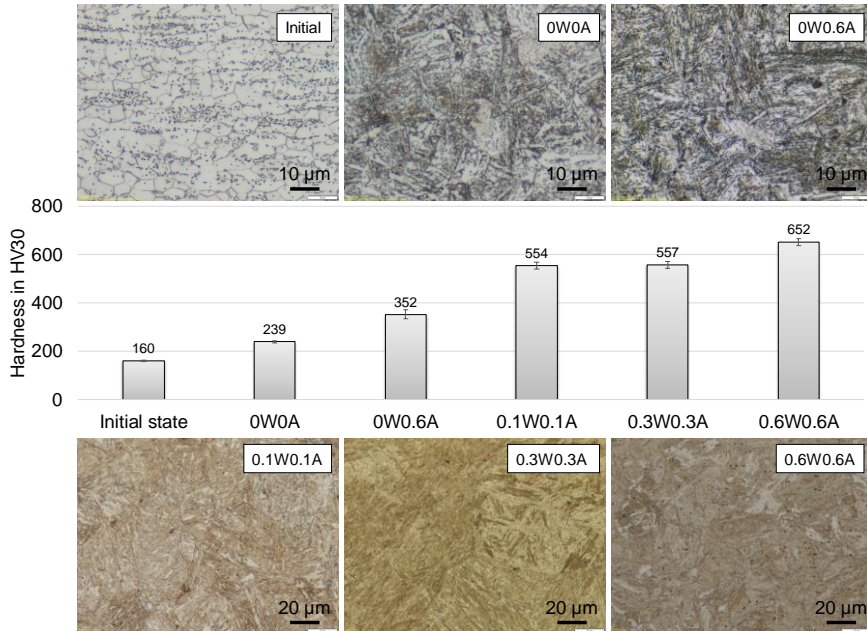


Fig. 10. Average hardness over the tube length of the given samples with respective optical micrographs.

Additionally, to control the homogeneity of the heat-treatment and hence of the mechanical properties over the cross-section, the hardness was measured in the transverse direction on some selected sections. In Fig. 11, the hardness is presented along the rotation, where 0/360° corresponds to the position of the weld seam.

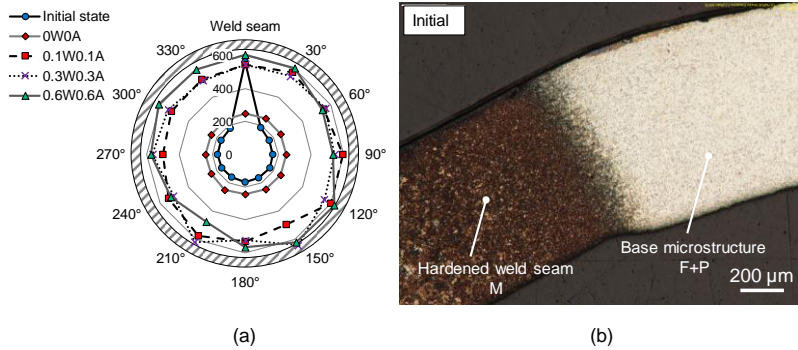


Fig. 11. (a) Average hardness along the tube cross-section as a function of rotation angle in reference to the weld seam for the given samples; (b) optical micrograph of the welded zone in the initial state without heat-treatment (M – martensite, F – ferrite, P – perlite).

The course of the initial state stands out from the rest due to a hardness jump that corresponds to the weld seam. The hardness in this point correlates with the hardened samples that suppose martensite formation in the seam (Fig. 11b). Interestingly, the influence of welding is completely eliminated due to the heat-treatments, which becomes evident by comparing the initial state against the air cooled state 0W0A, which exhibits the homogeneous course over the whole cross-section. The water-air quenched samples feature less homogenous cross-section properties with a certain value scatter. However, the hardness remains above 500 HV, which implies a martensitic microstructure in the whole cross-section for the water-air cooling.

Non-destructive microstructure characterization

Destructive methods of the mechanical or microstructure analysis, e.g. hardness measurement, tensile testing or microscopy, usually require appropriate surface conditions and/or preparation of standard samples, which is time- and cost-consuming. From this point of view, non-destructive analyses appear to be beneficial. These can be adapted for a microstructure characterization as well.

Hence, magnetic measurements of magnetization and demagnetization of the manufactured samples were performed. Under the influence of a magnetic field, ferromagnetic materials create a characteristic hysteresis loop that plots the generated magnetic flux B or in some cases magnetization M over the applied magnetic field H [25]. The hysteretic form is caused by the irreversible magnetic behavior of the ferromagnetic materials [26]. This means that, once a material is magnetized with a certain magnetic field, a higher opposite magnetic field has to be applied in order to demagnetize it. To characterize the magnetic hysteresis, four values are

mostly handled: energy losses that are defined by the hysteresis area A ; coercive force H_C that represents a value of the magnetic field strength at $B=0$; remanence B_r that is equal to the magnetic flux at $H=0$ and the saturated magnetic flux B_s (Fig. 12). Here, the energy losses and the coercive force were analyzed in terms of their correlation with the mechanical properties.

The steel phases with exception of austenite are known for their ferromagnetic properties at room temperature [27, 28]. Herewith, ferrite exhibits so called soft magnetic properties that are defined by relatively low coercive forces and energy losses; martensite belongs to the hard magnetic materials with high values of these properties [29]. Similarly to the mechanical properties, the magnetic properties of bainite cover a range of values between ferrite and martensite in dependence on the amount of carbide precipitations. Austenite is paramagnetic and hence, does not create a hysteresis loop under a magnetic field [28]. Due to the low carbon content in 22MnB5, the presence of retained austenite at room temperature is rather unlikely [13].

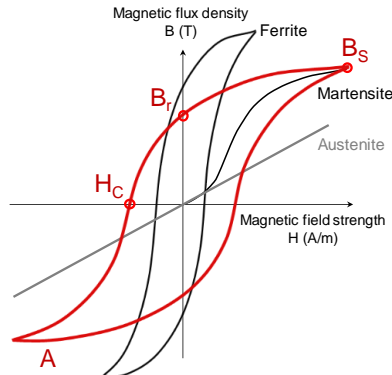


Fig. 12. Typical magnetization hysteresis loops of the steel phases in the coordinate system of magnetic field and flux density with definition of characteristic magnetic values.

The magnetic properties of the manufactured samples were determined using a power supplier from Kepco and an experimental magnetic device (Fig. 13). It consists of a primary coil (H-coil) with 91 turns to create a magnetic field with help of alternate current generated by the power supplier. Another component is a secondary coil (B-coil) with 23 turns to pick up the created electromotive force. To close the magnetic circuit and decrease the macroscopic demagnetizing field, the tube sample was assembled with a ferrite yoke of an adapted shape. Measurements were carried out with an interval 10 mm in the longitudinal direction of the tube. 10 cycles of magnetization per measurement were performed for a statistical evaluation with a current frequency of 2 Hz. Values of the applied current and the generated voltage were recorded. They were transformed into values of the magnetic field and flux according to Ampere's and Lenz's-Faraday laws under consideration of the geometry of the setup and samples as well as parameters of H- and B-coils.

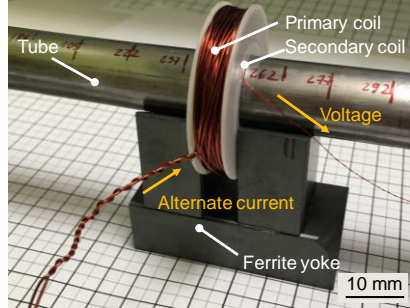


Fig. 13. Setup of the magnetic device composed for determination of the magnetic properties in the tube cross-sections.

Hysteresis loops for each measured spot served for determination of the coercive force and energy losses. Magnetic properties of the characteristic samples, namely 0W0A, 0.6W0.6A and of the initial state are exemplary depicted in Fig. 14. Their dependence on the heat-treatment and the phase composition is evident. The initial state, namely ferrite-perlite, exhibits a slim hysteresis with a high level of magnetization. In contrast, the magnetization behaviors of 0W0A and 0.6W0.6A look more similarly due to the macroscopically identical values of the maximal magnetic flux; however, 0.6W0.6A exhibits a noticeable higher coercive force and hence, higher total energy losses.

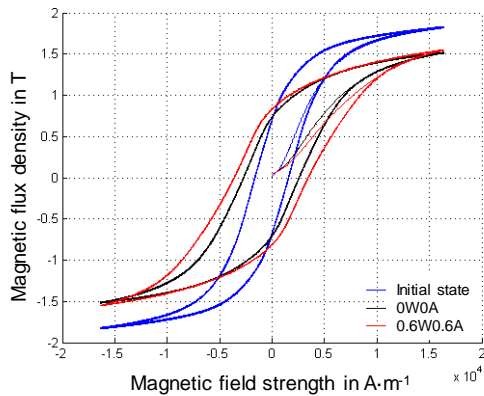


Fig. 14. Hysteresis loops of the exemplary cross-sections from the given samples.

The evaluation of the whole measure data reveals a general dependence of the magnetic properties on the cooling intensity. Fig. 15 illustrates average values of the energy losses and the coercive force over the applied cooling and the initial state as a reference correspondingly. Both values increase continuously with a cooling intensity and reach their maxima at the water-air cooling with 0.1 MPa; then they exhibit a slight decrease. Three ranges that represent three general states (initial, air

cooled and water-air cooled) can be clearly distinguished by the values of the magnetic properties.

Within the water-air cooling, it is remarkably that the magnetic properties show a slightly inverse relation to the cooling intensity in contrast to the hardness values (cf. Fig 10) and to the literature [27]. The coercive force is often called “magnetic hardness”, since it is similarly influenced by the microstructure [25]. Interactions between the magnetic constituents as magnetic walls or domains and the microstructure as stress fields or dislocations are responsible for this connection [26]. In these investigations, a more intense cooling seems to induce internal stresses in the microstructure that could lead to the decrease of the magnetic properties.

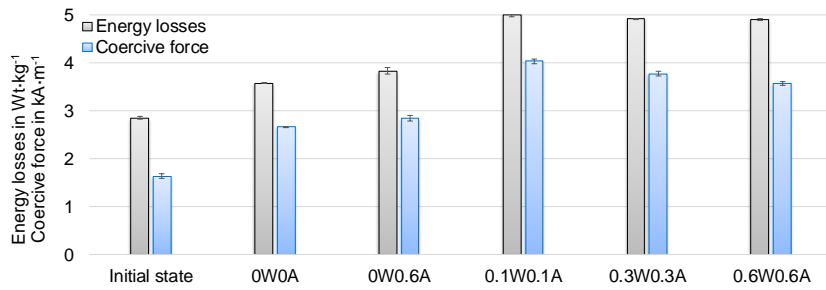


Fig. 15. Average values of the energy losses and coercive force for the given samples with standard deviation.

With the aim of a non-destructive prediction of the phase composition, a correlation between the mechanical and magnetic properties was derived. In Fig. 16, hardness was plotted as a function of the energy losses (Fig. 16a) and the coercive force (Fig. 16b) in the whole range of the measured data. It can be seen that their interactions can be described with exponential functions $HV = 30.237 \cdot e^{0.60114}$ ($R^2 = 0.969$) and $HV = 64.353 \cdot e^{0.5733H_C}$ ($R^2 = 0.946$). The data of 0.6W0.6A deviate more pronounced from the exponents, which might be explained by the increased internal stresses described above. This phenomenon will be studied more precisely in the following works.

The obtained dependencies allow the prediction of the mechanical properties on basis of the non-destructive analysis.

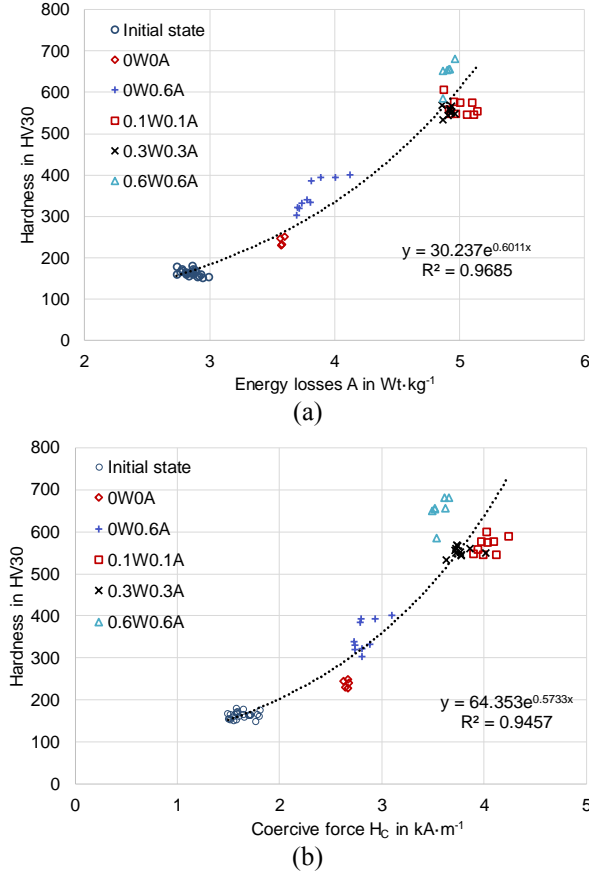


Fig. 16. Hardness of the given samples as a function of energy losses A (a) and coercive force H_c (b) with respective logarithmic equations.

Virtual design of tube heat-treatment

A numerical simulation of the technological process can substitute numerous experimental tasks and efforts. Thus, a suited mathematical model was developed and implemented in the simulation software ANSYS Workbench. The model allows for a prediction of the mechanical properties of the finished product and an inverse determination of the technological input parameters of the heat-treatment in terms of intended mechanical properties (Fig. 17) [30].

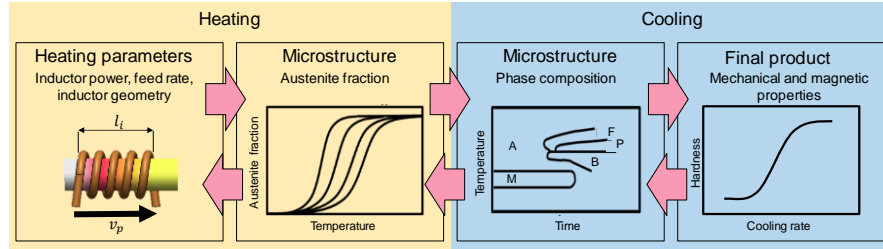


Fig. 17. Model allowing the inverse determination of the required parameters of heat-treatment based on target mechanical properties.

For the simulation of the heat-treatment, an electromagnetic task of the energy losses during inductive heating and a thermal task of the temperature evolution and corresponding phase transformations during heating/cooling has to be solved. In ANSYS, both tasks are considered separately by Maxwell eddy current and thermal solvers respectively with a direct coupling of the results via the so-called Response Surface Optimization tool and the feedback operator. The virtual feed and tube movement are achieved by the prescribed time intervals for the heating/cooling that were defined by the given feed rates and geometrical parameters of the heat-treatment station.

During the inductive heating a magnetic field created by the alternating current generates heating energy in a conductor (herein – tube). Flowing through the tube body, it induces ohmic losses that serve as a heat source. The distribution of the electric field and hence, heat flow over the volume of the conductor depends on the physical properties of the material. The energy losses and heat distribution induced by the inductive heating were included in the developed model by simulating the high-frequency alternating current. The geometrical and material parameters of the induction coil and the tube body were taken from the experimental setup (cf. Fig. 2). The physical properties of 22MnB5 were based on literature data [10, 31, 32] and modelled temperature dependent. In order to take the Curie temperature and hence, the change of the magnetic properties into account, a finite number of calculation steps within the steady-state task was specified with prescribed intervals of heating time. Temperature values calculated at each processing step were implemented as boundary conditions for each subsequent step. Although a decreasing time step size increases the quality of the model, the number of time steps should be minimized due to significant time and processing efforts. For the current simulation, 20 time steps of 0.1 s were used and the simulation was carried out according to the experimental conditions and parameters of the inductive heating (see p. 12).

Ohmic losses calculated in the electromagnetic solver were transferred into the thermal solver and the transient thermal analysis of the phase transformations was performed. Automatic adaptive meshing was applied to efficiently determine ohmic losses and fix the skin layer thickness providing a higher accuracy of calculations according to [33]. The ohmic losses averaged over the elements were defined as a spatially distributed loads. This allowed to determine the heat flow and the corresponding temperature distribution field (Fig. 18).

According to the generated temperature field evolution and the transformation kinetics described by the JMA-equation (Fig. 6), the amount of formed austenite was calculated for each element (Fig. 18).

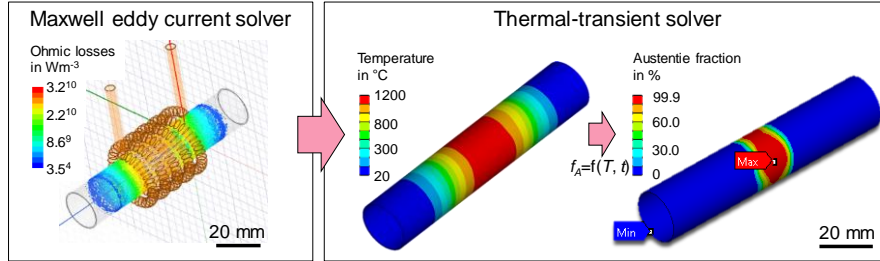


Fig. 18. Simulation of the inductive heating for a feed rate of 16.7 mm s^{-1} composed of the determination of ohmic losses due to inductive influence in Maxwell eddy current solver and generation of the temperature field along with calculation of the austenite fraction in the thermal-transient solver.

Based on the computed austenite fraction, its decomposition into martensite during the subsequent cooling was considered. The cooling process was divided into two stages: passive air cooling during transportation and active spray cooling with a water-air mixture at water-air pressures of 0.1 MPa. According to the experimental data, this configuration ensures a complete transformation of austenite into martensite, thus diffusive transformations were not considered. The heat transfer coefficients for these cooling conditions were modelled temperature dependent according to preliminary investigations. Based on the temperature evolution, the phase transformations during the cooling were described for each mesh element according to Wildau-Hougardy [34]:

$$f_M = 1 - \exp[-\gamma(M_s - T)]^\zeta, \quad (6)$$

where f_M - martensite fraction; T - temperature at a particular time in $^{\circ}\text{C}$; M_s - initial temperature of martensite transformation in $^{\circ}\text{C}$; γ , ζ - material coefficients (depend on the M_s). The start temperature of martensite transformation was defined considering the actual chemical composition of 22MnB5 [35].

The phase distribution along the tube after the heating (a), during the cooling (b) at a time point of 19.5 s, when martensite is partially formed, and after the full cooling (c) are plotted in Fig. 19. At the beginning of the cooling, the heated part consists completely of austenite, non-heated parts are ferritic-perlitic and a transition zone of the partial austenitizing is present. After the reaching the martensite start temperature, the martensite begins to form. In Fig. 19b, an increasing fraction of martensite is visible. A slight asymmetric formation is a consequence of the non-homogeneous distribution of ohmic losses. It becomes more evident during the transformation, when slightly different ohmic losses result in a visible difference of the phase transformation. Furthermore, the martensite fraction slightly decreases from the transi-

tion zone towards the center due to the occurring temperature gradient (the transition zone cools faster due to the heat flow towards the non-austenized tube sections). Thus, for this point of time, the martensite fraction is higher close to the transition zone, than in the center. With temperature alignment, the difference of martensite fraction continuously decreases and is eliminated, when the transformation is completed (Fig. 19c).

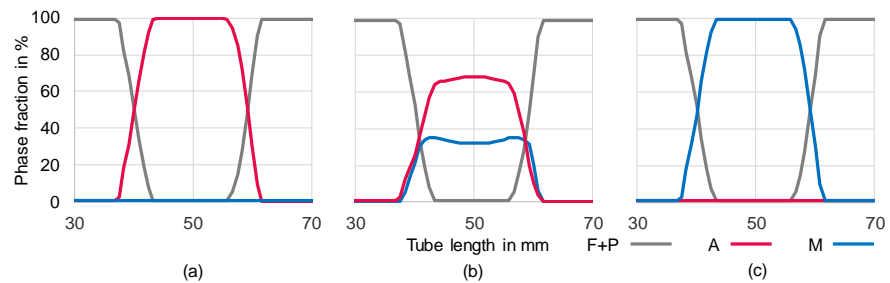


Fig. 19. Phase distribution along the tube length on the inner tube surface after the inductive heating (a), at the time point of 19.5 s during the cooling (b) and after the completed cooling (c).

The developed model simplifies experimental efforts by the available interconnection of different model elements in ANSYS Workbench. It allows determining of suited process parameters for designated properties of the finished product.

Conclusions

A technological process for the continuous manufacturing of tubes from the boron-alloyed steel 22MnB5 featuring tailored properties in the longitudinal direction was developed. A continuous tube forming line was upgraded with a heat-treatment station composed of a short-action inductive heating and flexible water-air spray cooling system. In terms of control over the transformation kinetics during the fast heating and cooling under consideration of the technological parameters, investigations on austenitizing and austenite decomposition were performed. The results can be summarized as follows:

- Dilatometric experiments on nominal inductive heating at rates from 500 K s^{-1} to 2500 K s^{-1} resulted in a complete austenitizing of all investigated samples. Since the actual heating rates in the relevant two-phase region were lowered to $368 \text{ K s}^{-1} - 380 \text{ K s}^{-1}$ due to the change of the magnetic properties, the transformation kinetics of austenite formation appears to be similar for all experiments. However, the influence of the increasing heating rates, which were equal to the target ones up to Curie temperature, is expressed by the shift of the transfor-

mation temperatures to higher values and enlarging of the transformation temperature range. Austenite formation was described as a function of temperature and heating time by a JMA-model.

- The heat-treatments performed in the developed technological line revealed that a wide range of phase compositions and mechanical properties can be obtained by varying the cooling parameters. The cooling with still as well as compressed air resulted in a complex microstructure consisting of ferrite, lower and upper bainite with hardness values of 239 HV and 352 HV respectively. The austenitized samples exposed to the water-air cooling exhibited quenched microstructure with an average hardness above 550 HV.
- Magnetic properties evaluated for the nondestructive characterization of the mechanical properties of the heat-treated tubes showed a clear dependency on the cooling conditions. Using logarithmic functions, the mechanical properties can be predicted based on values of energy losses and coercive force.
- ANSYS Workbench was applied to simulate the heat-treatment process and to predict the mechanical tube properties. Therefore, the temperature field was computed based on values of ohmic losses, which served as a heating source. Based on dilatometric measurements, the evolution of austenite formation was described by a JMA-model. Subsequently, austenite decomposition due to transformation of the prior austenitized material sections into martensite was computed.

Acknowledgments The present study is funded by the Deutsche Forschungsgemeinschaft (DFG, German Research Foundation) – project number 134839507 within the scope of the graduate school’s IRTG 1627 “Virtual Materials and Structures and their Validation”, subproject C5 “Virtual Design and Manufacturing of Tailored Tubes”.

References

1. Merklein M, Johannes M, Lechner M et al (2014) A review on tailored blanks — Production, applications and evaluation, *J Mater Process Technol* 214:151–164.
2. Zadpoor AA, Sinke J, Benedictus R (2007) Mechanics of tailor welded blanks: an overview. *Key Eng Mater* 344:373–382.
3. Groche P, Wohletz S, Brenneis M et al (2014) Joining by forming – A review on joint mechanisms, applications and future trends. *J Mater Process Technol* 214(10):1972–1994.
4. Kopp R, Wiedner C, Meyer A (2005) Flexibly rolled sheet metal and its use in sheet-metal forming. *Adv Mater Res* 6(8):81–92.
5. Vollerstsen F, Lange K (1998) Enhancement of drawability by local heat treatment. *CIRP Ann Manuf Technol* 47:181–184.
6. Geiger M, Merklein M, Vogt U (2009) Aluminium Tailored Heat Treated Blanks. *Ann Ger Acad Soc Prod Eng WGP* 401–410.
7. Chang Y, Wang CY, Zhao KM et al (2016) An introduction to medium-Mn steel: Metallurgy, mechanical properties and warm stamping process, *Mater Des* 94:424–432.
8. Naderi M, Durrenberger L, Molinari A et al (2008) Constitutive relationships for 22MnB5 boron steel deformed isothermally at high temperatures. *Mater Sci Eng A* 478:130–139.

9. Karbasian H, Tekkaya AE (2010) A review on hot stamping. *J Mater Process Technol* 210:2103-2118.
10. Spittel M, Spittel T (2009) Steel symbol/number: 22MnB5/ 1.5528. In: Warlimont H (ed.) Springer Materials – The Landolt-Bornstein Database, Springer-Verlag Berlin Heidelberg. DOI: 10.1007/978-3-540-44760-3_146
11. Herbst S, Steinke KF, Maier HJ et al (2016) Determination of heat transfer coefficients for complex spray cooling arrangements. *Int J Microstruct Mater Prop* 11:229-246.
12. Merklein M, Lechler J (2008) Determination of material and process characteristics for hot stamping processes of quenchable ultra high strength steels with respect to a FE-based process design. *SAE World Congress: Innovations in Steel and Applications of Advanced High Strength Steels for Automobile Structures 2008–0853*. DOI: 10.4271/2008-01-0853.
13. Naderi M, Saeed-Akbari A, Bleck W (2008) The effects of non-isothermal deformation on martensitic transformation in 22MnB5 steel. *Mater Sci Eng A* 487:445-455.
14. Guk A, Kunke A, Kräuse V et al (2017) Influence of inductive heating on microstructure and material properties in roll forming processes, *AIP Conf Proceed*, 1896:800271-800276.
15. Tröster T, Niewel J (2014) Inductive heating of blanks and determination of corresponding process windows for press hardening. *Report Project P 805 / IGF-Nr.16319 N*.
16. Hordych I, Bild K, Boiarkin V et al (2018) Phase transformations in a boron-alloyed steel at high heating rates. *Proced Manuf* 15:1062-1070.
17. Haimbaugh R (2015) Practical induction heat treating, 2nd edn. ASM International, ISBN 9781627080897.
18. Kolleck R, Veit R, Merklein M et al (2009) Investigation on induction heating for hot stamping of boron alloyed steels, *CIRP Ann Manuf Technol* 58:275–278.
19. Miokovic T, Schwarzer J, Schulze V et al (2004) Description of short time phase transformations during the heating of steels based on high-rate experimental data. *J Phys IV* 120:591-598.
20. Kuepferle J, Wilzer J, Weber Set al (2015) Thermo-physical properties of heat-treatable steels in the temperature range relevant for hot-stamping applications. *J Mater Sci*, 50:2594-2604.
21. Johnson WA, Mehl RF (1939) Reaction kinetics in process of nucleation and growth. *Trans Metall Soc AIME* 135:416–458.
22. Avrami M (1941) Kinetics of phase change. *J Chem Phys* 9:177-184.
23. Nowak M, Golovko O, Nürnberg F et al (2013) Water-Air Spray Cooling of Extruded Profiles: Process Integrated Heat Treatment of the Alloy EN AW-6082. *J Mater Eng Perform* 22:2580-2587.
24. EN ISO 6507-1 (2005) Metallic materials – Vickers hardness test – Part 1: Test method.
25. Morgner W, Michel F, Bezljudko G et al (2015) Zerstörungsfreie Materialcharakterisierung mittels Koerzimetrie. *Non-Destr Test J* 144:40-43.
26. Hubert O, Lazreg S (2017) Two phase modeling of the influence of plastic strain on the magnetic and magnetostrictive behaviors of ferromagnetic materials. *J Magn Magn Mater* 424:421-442.
27. Byeon JW, Kwun SI (2003) Magnetic evaluation of microstructures and strength of eutectoid steel. *Mater Trans* 44(10):2184-2190
28. Nahak B (2017) Material characterization using Barkhausen noise analysis technique - a review. *Indian J Sci Technol* 10(14):1-10.
29. Saquet O, Chicois J, Vincent A (1999) Barkhausen noise from plain carbon steels: analysis of the influence of microstructure. *Mater Sci Eng A* 269:73-82.
30. Hordych I, Boiarkin V, Rodman D et al (2017) Manufacturing of tailored tubes with a process integrated heat treatment. *AIP Conf Proc* 1896:1900031-1900036.
31. Vibrans T (2016) Induktive Erwärmung von Formplatten für die Warmumformung. Doctoral Thesis, Chemnitz.
32. Zedler T, Nikanorov A, Nacke B (2008) Investigations of relative magnetic permeability as input data for numerical simulation of induction surface hardening. *Proceed Int Scientific Colloquium Modelling for Electromagnetic Processing* 119-126.

33. Larsen P, Horiuchi T (2013) Induction heating applications. ANSYS Application Brief. <https://www.ansys.com/-/media/ansys/corporate/resourcelibrary/techbrief> (downloaded on 25.10.18)
34. Wildau M, Hougardy H (1987) Zur Auswirkung der Ms-Temperatur auf Spannungen und Maßänderungen. J Heat Treat Mater 42:261-268.
35. Hochholdinger B (2012) Simulation des Presshärteprozesses und Vorhersage der mechanischen Bauteileigenschaften nach dem Härteten. Doctoral thesis, Stuttgart.